The Planetary Science Journal, 3:217 (14pp), 2022 September https://doi.org/10.3847/PSJ/ac8c39

The Contribution of Small Impact Craters to Lunar Polar Wander

David E. Smith[1,5], Vishnu Viswanathan[2,3,5], Erwan Mazarico[3], Sander Goossens[3], James W. Head[4], Gregory A. Neumann[3], and Maria T. Zuber[1]
[1] Department of Earth, Atmospheric and Planetary Sciences, Massachusetts Institute of Technology, Cambridge, MA 02139, USA; smithde@mit.edu
[2] Center for Space Sciences and Technology, University of Maryland Baltimore County, Baltimore, MD 21250, USA; vishnu.viswanathan@nasa.gov
[3] Solar System Exploration Division, NASA Goddard Space Flight Center, Greenbelt, MD 20771, USA
[4] Department of Earth, Environmental and Planetary Sciences, Brown University, Providence, RI 02912, USA
Received 2022 April 15; revised 2022 July 12; accepted 2022 August 19; published 2022 September 19

Abstract

Changes in mass distribution affect the gravitational figure and reorient a planetary body's surface with respect to its rotational axis. The mass anomalies in the present-day lunar gravity field can reveal how the figure and pole position have evolved over the Moon's history. By examining sequentially each individual crater and basin, working backward in time order through the catalog of nearly 5200 craters and basins between 1200 and 20 km in diameter, we investigate their contribution to the lunar gravitational figure and reconstruct the evolution of the pole position by extracting their gravitational signatures from the present-day Moon. We find that craters and basins in this diameter range, which excludes South Pole–Aitken, have contributed to nearly 25% of the present-day power from the Moon's degree-2 gravitational figure and resulted in a total displacement of the Moon's pole by ∼10° along the Earth–Moon tidal axis over the past ∼4.25 billion years. This also implies that the geographical location of the Moon's rotational pole has not moved since ∼3.8 Ga by more than ∼2° in latitude owing to impacts, and this has implications for the long-term stability of volatiles in the polar regions.

Unified Astronomy Thesaurus concepts: The Moon (1692); Lunar evolution (952); Lunar gravitational field (956); Lunar geodesy (955); Planetary polar regions (1251); Impact phenomena (779); Lunar impacts (958); Planetary structure (1256); Planetary dynamics (2173)

1. Introduction

The Moon preserves the record of its bombardment in its gravity and topography, which have been mapped at high resolution by the Gravity Recovery and Interior Laboratory (GRAIL) mission (Asmar et al. 2013; Zuber et al. 2013b) and the Lunar Orbiter Laser Altimeter (LOLA) on board the Lunar Reconnaissance Orbiter (LRO) mission (Chin et al. 2007; Smith et al. 2010a), respectively. These two data sets have revealed the precise size and distribution of lunar craters (Head et al. 2010) and their associated gravity anomalies (Neumann et al. 2015).

Gravitational features alter the moments of inertia of planetary bodies and thus influence their orientation and rotation. The Moon's reorientation that stems from large impact events results from two effects—a transient stage followed by a secular one (Melosh 1975). In the transient stage, the impact itself transfers torque to the angular momentum of the Moon, resulting in a potentially short-lived nonsynchronous rotation that spans less than a few hundred years (Keane et al. 2017). In the secular stage, post-impact changes to the mass distribution (i.e., intrusion and extrusion of magmatic material; rebound of the mantle, crust, and lithosphere; etc.) cause a reorientation of the Moon toward its new minimum rotational energy configuration. This secular component does not move the rotational pole in inertial space but reorients the body and surface relative to the rotation pole to minimize the energy required to maintain the spin. This secular reorientation arises primarily from centrifugal forces acting on the nonuniform mass distribution, on the surface or within the quasi-rigid body, pushing excess masses toward the equator and mass deficiencies toward the nearest pole (Evans 2002). Here we refer to this phenomenon as "true polar wander," or "polar wander" for short. This paper investigates the Moon's polar wander using gravitational models of basins and craters obtained from today's lunar gravity field.

The Moon's polar wander has been studied extensively in the past, and discussions of previous research can be found in Melosh (1975), Bills (1995), Matsuyama et al. (2014), Keane & Matsuyama (2014), Takahashi et al. (2014), and Matsuyama et al. (2021), for example. In addition, several lunar paleopoles were published in just the past decade based on the study of topographical features (e.g., Garrick-Bethell et al. 2014), paleomagnetism (e.g., Nayak et al. 2017), and epithermal neutron observations (e.g., Siegler et al. 2016). As a result of the improved lunar topographic and gravity models (Zuber et al. 2013a; Smith et al. 2010b), geophysical models of individual large craters and basins have been developed (e.g., Garrick-Bethell et al. 2014; Keane & Matsuyama 2014), from which a change in the pole position was derived. However, there is a lack of consensus concerning the position of lunar paleopoles, which can be due to the accuracy, reliability, and completeness of the data used; to other inherent model assumptions (such as axial dipole hypothesis used for magnetic paleopoles); and to the differences in epochs associated with them. Our work aims to improve the completeness of the data used in the estimation of lunar paleopoles and to provide a time evolution of the lunar paleopole by relying directly on a high-accuracy, high-resolution solution of the GRAIL lunar gravity field.

The largest scales of the gravity field, represented by the low-degree spherical harmonics (SH) coefficients (Kaula 1966),

[5] These authors contributed equally to this work.

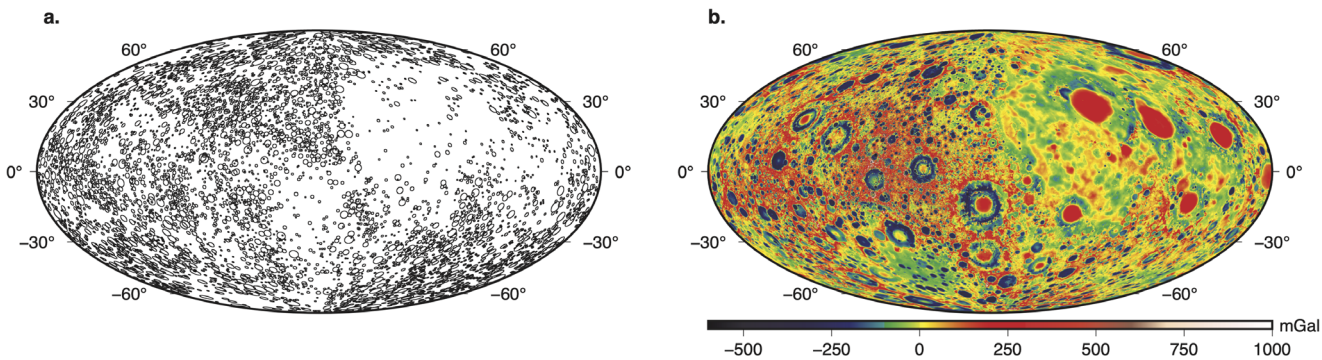

Figure 1. (a) Hammer projection map centered on 270° E showing the nonuniform distribution of craters with diameter 20–150 km (Head et al. 2010; Neumann et al. 2015). (b) Map of lunar gravity anomalies expanded to degree and order 650 (GRGM1200B solution; Goossens et al. 2020).

dictate the equilibrium orientation of a planetary body. Large impactors, fewer in number, have left large gravitational anomalies, while the more numerous smaller impactors each contributed smaller individual gravitational anomalies. Previous studies based on lunar topographic and gravity models (Garrick-Bethell et al. 2014; Keane & Matsuyama 2014; Matsuyama et al. 2021) did not consider the compounded effect of the small features (with $D \lesssim 200$ km, where D is the diameter), and instead these were either not considered or deemed negligible compared to the larger craters and basins. Our study includes an estimation of both the individual and the cumulative effect of craters and basins down to 20 km in diameter, in terms of their contribution to the degree-2 gravity field of the Moon and thus to the gravitational figure and polar wander history.

In this paper, we account for the contribution of basins and craters down to 20 km in diameter. The inclusion of small craters is motivated by their large number, their nonuniform distribution (Figure 1(a); see also the discussion in Section 3.2), and their potentially significant cumulative effect on the lunar low-degree gravity field. Our catalog, which we refer to as SV22, comprises 5184 craters and basins from Head et al. (2010) and 13 basins from Neumann et al. (2015). This constitutes a near-exhaustive list of impact features from 1200 to 20 km in diameter. We model their gravity signature with the recent GRAIL gravity model GRGM1200B (Goossens et al. 2020; Figure 1(b)) and extract the gravity signals for each individual anomaly from today's lunar gravity field. While our approach is capable of estimating the contribution of the South Pole–Aitken (SPA) basin, we exclude it from the true polar wander analysis of this study owing to the large range of possible SPA models that satisfy its gravitational signal, particularly due to uncertainties associated with the origin, extent, asymmetry, and volume of its heavily cratered ejecta deposit. Previous studies that considered SPA's contribution to polar wander (Keane & Matsuyama 2014; Matsuyama et al. 2021) show large differences in its low-degree gravity contribution (Table 1), as well as their paleopole estimates. Given that SPA is generally assumed to be the oldest impact feature on the Moon, our reconstruction of the polar wander evolution remains valid from the SPA impact forward in time.

We perform our polar wander analysis in three steps. First, we generate the models of craters and basins based on a sequential modeling technique (Section 2.1). Second, these models are arranged in an ensemble of time-ordered sequences consistent with the best-known cratering chronology

Table 1
Estimates of the Degree-2 Gravity Coefficients (Unnormalized) of South Pole–Aitken from Different Studies Show High Variance

Spherical Harmonics Coefficients						Reference
C_{20}	C_{21}	C_{22}	S_{21}	S_{22}	($\times 10^5$)	
−5.67	−7.06	−2.01	−1.31	−0.82		Keane & Matsuyama (2014)
−11.30	−3.05	1.81	0.05	4.41		Matsuyama et al. (2021)
−3.82	−3.71	−0.64	−0.65	−0.23		This study[a]

Note.
[a] As per modeling described in Section 2.1.

(Section 2.2). Third, the contributions of the craters and basins to the Moon's moment of inertia tensor are sequentially subtracted and the Moon reoriented at each step (Section 2.3). Our sequential methodology considers (a) the cratering and reorientation history and their combined influence on the polar wander path taken by the Moon from its present-day pole position to its paleopole at ∼4.25 Ga, and (b) modifications of the final paleopole due to changes in the strength of equilibrium rotational and tidal bulges from the Moon's tidal recession, i.e., if a crater impacts at a time when the Moon had a faster spin and closer distance to Earth, it would have to overcome a higher rotational stability than if the same crater had impacted at times of slower spin and lower tidal interaction and associated lower rotational stability (here stability refers to the increased resistance to polar wander due to the action of the tidal and rotational bulges). During polar wander, the relative location of a crater changes with respect to the instantaneous equilibrium rotational and tidal bulges (see Figure 1 in Matsuyama et al. 2014) owing to the (partial) readjustment of these bulges after the reorientation caused by an earlier crater in the sequence. Thus, we evaluate the contribution of each crater and basin based on this relative location, taken at the time of impact. The relative distance between craters, however, is kept fixed owing to the absence of any observed, present-day or past surface plate tectonics on the Moon (Shapiro et al. 2021; Williams & Boggs 2021). The three-step process enables us to determine the Moon's polar wander path with associated geological time stamps (Section 3). Comparisons with prior works, potential sources of uncertainties in our analysis, and topics for future work are discussed (Section 4), followed by concluding remarks and takeaways of our study (Section 5).

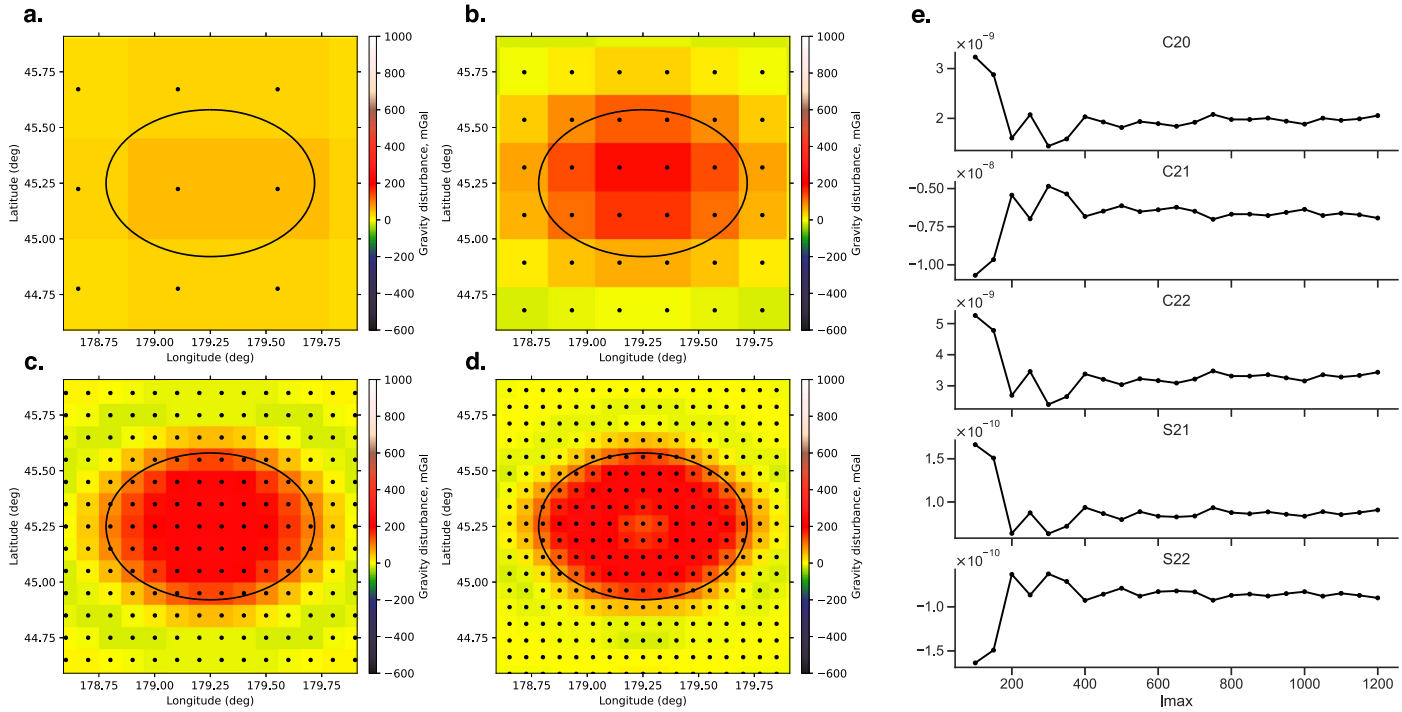

Figure 2. Spatial sampling of a typical crater at various resolutions (panels (a)–(d): SH degrees 200, 420, 900, 1200). Panel (e) shows the effect of the SH resolution on the determination of the degree-2 coefficients.

2. Methodology

2.1. Gravity Field Modeling of Craters

We developed an approach to derive the gravity fields of individual craters and basins using their locations from the SV22 catalog in the present-day lunar principal axis (PA) coordinate system. We computed the free-air gravity anomaly from GRGM1200B, which has an effective spatial resolution of ∼8 km (SH degree 650–700; Goossens et al. 2020). We determine the SH representation for each feature using SH transforms. We isolate the feature (see below) on a global map, with all gravity values equal to zero, except for the feature itself, and then transform this into SH. Determining the low-degree gravity contribution of a crater using too coarse a resolution when sampling this map (fewer samples spatially) can induce large errors. To avoid such biases, we determine the SH representation for each gravity anomaly to degree and order $L = 1200$, equivalent to ∼5 km spatial resolution at the lunar equator, which provides several tens of samples over a 20 km crater and its immediate ejecta deposit. Figure 2 shows different samplings and how they affect the determination of the degree-2 coefficients. Figure 2(e) shows the need to expand the fields at least beyond degree 400, and arguably degree 600, to ensure convergence in the determination of the degree-2 coefficients.

Each SV22 feature was sampled along 360 azimuthal directions up to a distance of two crater radii. These profiles were averaged to obtain the azimuthally averaged crater gravity signature. The background gravity of the surrounding area, obtained by averaging the values for $r_i > 1.25R_i$, was subtracted from this radial profile to prevent any discontinuity in the gravity map after the crater was removed, where r_i is the radial distance from the crater center and R_i is the crater radius. The choice of the 1.25 factor is empirical in origin, and its small sensitivity is discussed in Section 4. This corrected profile was interpolated onto a 0.06125°-resolution global grid to obtain the individual crater's gravity field, which was then converted to an SH expansion by computing the SH transform to $L = 1200$ (Wieczorek & Meschede 2018).

Figure 3 shows examples of four craters of different diameters, Mendel-Rydberg (636 km), d'Alembert (232 km), Shoemaker (51 km), and Shackleton (21 km), to illustrate our modeling. The figure shows the GRAIL gravity model GRGM1200B (left), the crater anomaly model (middle), and the gravity field after the computed crater anomaly has been removed (right). The modeling successfully removed the crater anomaly from the gravity field while retaining the remaining features in the region.

A measure of the effectiveness of our modeling is shown in Figure 4, where all 5197 craters are removed from the original gravity map. The impact features disappear visually; only the underlying long-wavelength signals remain. In addition, the method avoids any assumptions about the impactor in a forward-modeling approach (e.g., Matsuyama & Nimmo 2007).

Our primary interest is the set of degree-2 coefficients, as they relate to the moment of inertia tensor that defines the stable rotation configuration. We benchmark our modeling approach against the degree-2 estimates by Keane & Matsuyama (2014) and Keane et al. (2016) for the 29 large basins they considered. Our modeling matches 90% of their coefficient values within 3σ (Figure 5). We note that the agreement improves with decreasing crater size, with the smallest 16 craters all within 3σ.

The rationale for considering more than just the largest basins when studying polar wander is made clear by looking at the cumulative contribution of impact features to the overall degree-2 power. The gravitational power at degree-2 is independent of the coordinate system and thus a priori more robust to the exact polar wander evolution. That is, before our detailed orientation integration results (Section 3), degree-2 power can hint at

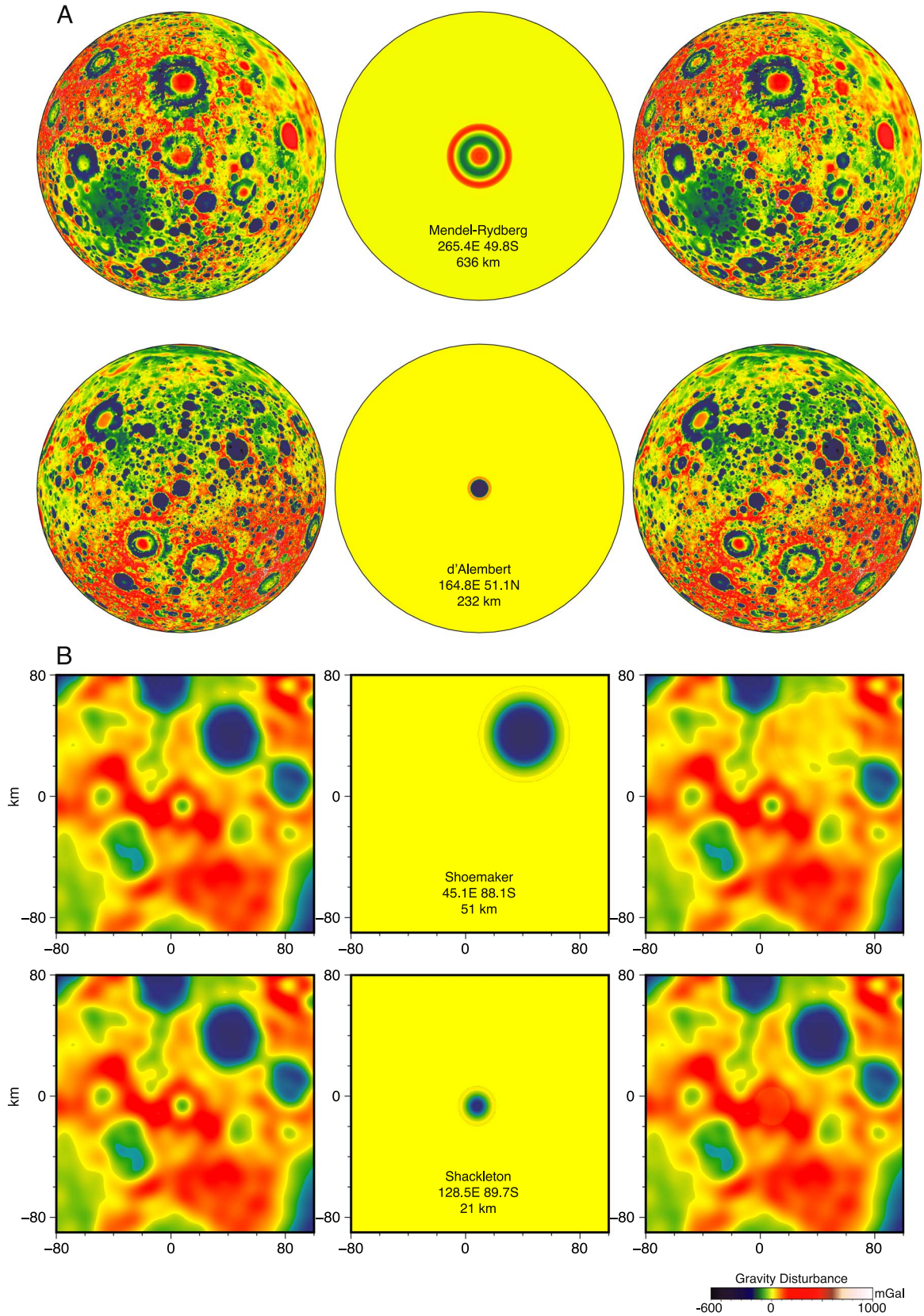

Figure 3. Examples of four craters, showing the GRAIL anomaly (left), the models (middle), and the gravity map after extraction of the models (right). The models effectively remove the primary signal but retain fine structure in the surrounding area. Projections are (a) orthographic and (b) stereographic (in km) centered at the crater location and the south pole, respectively.

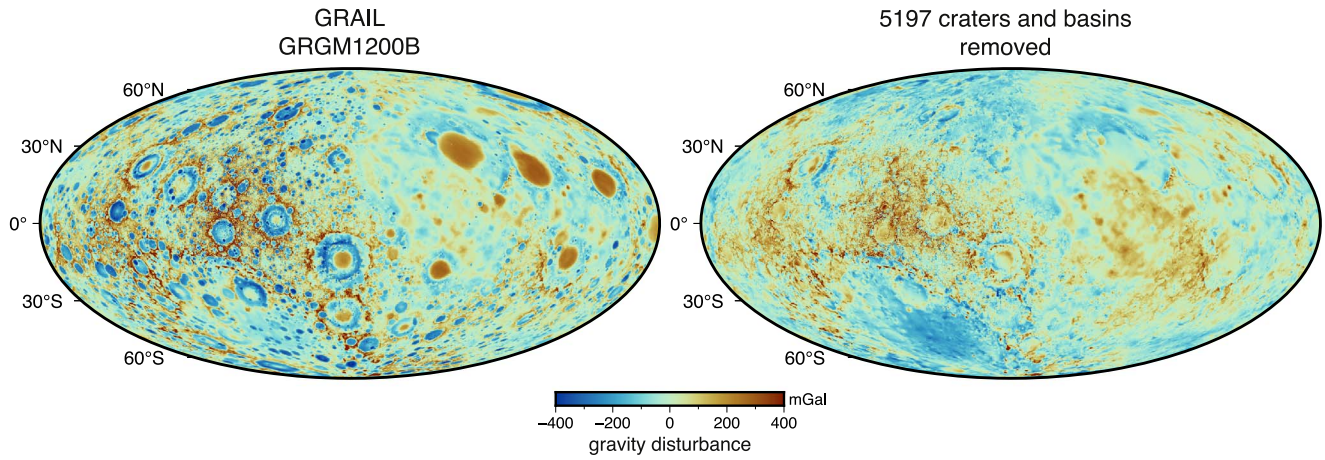

Figure 4. GRAIL gravity model GRGM1200B (left), and GRGM1200B with 5197 crater gravity anomalies removed (right).

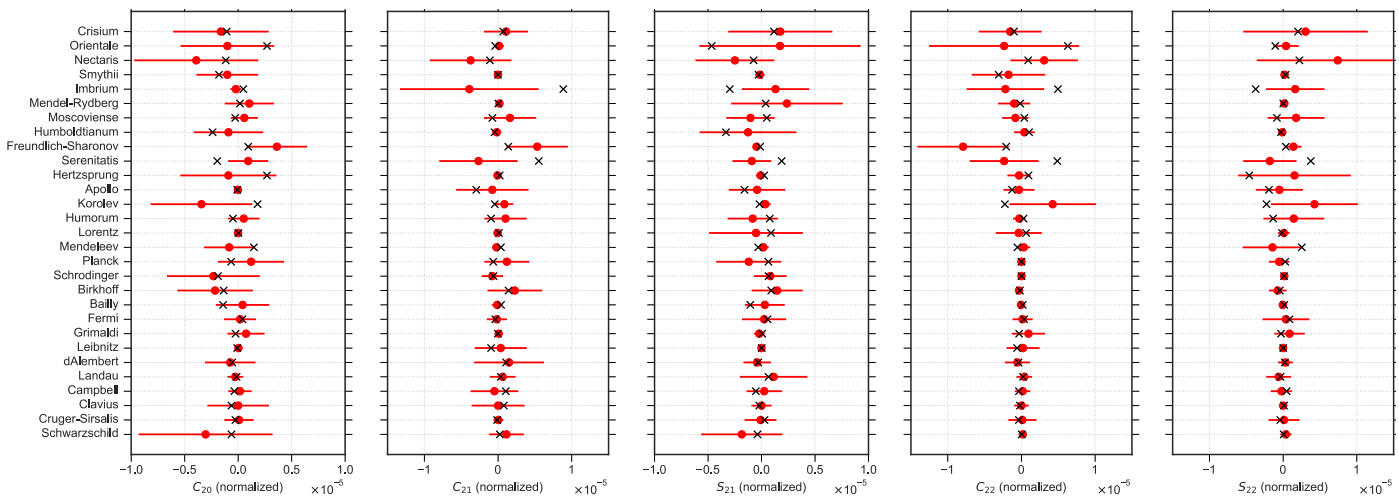

Figure 5. Comparison of coefficients of degree 2. The 29 values presented for large craters and basins in this paper show that 90% are within 3σ of the full set of craters and basins in Keane & Matsuyama (2014) and Keane et al. (2016), and 100% of the 16 smallest craters.

potential orientation changes stemming from the crater population. Despite small craters having minuscule degree-2 power individually (Figure 6(a), where $P_i = \sqrt{(\sum_m C_{2m,i}^2 + S_{2m,i}^2)}$), the cumulative power of craters smaller than 200 km is approximately half that of the entire catalog (Figure 6(b), where $P_{D_i} = \sqrt{(\sum_m (\sum_i^{D_i<D} C_{2m,i})^2 + (\sum_i^{D_i<D} S_{2m,i})^2)}$). Craters smaller than 200 km contribute ∼20% of the total degree-2 power of the Moon, while all 5197 SV22 craters amount to ∼35%. Given that the smallest feature in Keane & Matsuyama (2014) was Schwarzschild (207 km in diameter), this means that previous studies did not consider the majority of the degree-2 power.

2.2. Sequencing of Craters

To determine how cratering has affected the lunar degree-2 figure and polar wander over time, we need to establish an age sequence of the crater gravity anomalies. Since the age of each and every crater is not known, we leverage the best constraints when available and use a stochastic approach consistent with the geologic observations for the vast majority. For the largest craters, we assign ages from Fassett et al. (2012); for a set of 155 craters all greater than 200 km, we take the age (class) from Losiak et al. (2009); and for the remaining 5013 craters, we follow the crater density distribution function (e.g., Heiken et al. 1991; Neukum et al. 2001; Morbidelli et al. 2018).

Our resulting distribution of the entire SV22 catalog can then be classified into the six lunar geologic age classes: Copernican, Eratosthenian, Early Imbrian, Late Imbrian, Nectarian, and pre-Nectarian, numbered 6 to 1, respectively (Wilhelms et al. 1987). Table 2 shows the distribution for a typical randomized sequence we created. As mentioned above, the majority of craters are unassigned owing to the paucity of individual crater age information. In order to account for the stochastic nature of our sequencing method, we repeat this process multiple times and obtain an ensemble of statistically equivalent sequences, which we call draws. The validity of our results can be ascertained by their robustness across all these draws (Figure 7(a)).

An estimate of the time evolution of the degree-2 power of the Moon from its cratering chronology can then be obtained by iteratively subtracting the degree-2 coefficients of the modeled crater anomalies, ordered by their assigned ages in the SV22 catalog, from the present-day degree-2 gravity field of the Moon. Figure 7(b) shows such an estimate, using a single draw. This methodology enables the reconstruction of the degree-2 gravitational figure of the Moon from the bombardment history of the inner solar system. The early Moon after

SPA impact (at ∼4.25 Ga; Garrick-Bethell et al. 2020) is estimated to have a ∼25% smaller degree-2 power as compared to the present-day Moon, with a significant portion of this reduction occurring between post-SPA and Orientale basin formation. Additional consideration of our SPA model adds ∼12% to this estimate, giving the same total as in Figure 6(b). The time history of the degree-2 gravity field of the Moon enables an estimation of the paleopole path of the Moon, detailed in the following section.

2.3. Computation of True Polar Wander History

We represent the gravitational potential (U) due to the Moon evaluated at a point in spherical coordinates (r, θ, ϕ) as an SH series:

$$U(r,\theta,\phi)=\frac{GM}{r}+\frac{GM}{r}\sum_{l=1}^{\infty}\sum_{m=0}^{l}\left(\frac{R}{r}\right)^{l}P_{lm}\times(\cos\theta)(C_{lm}\cos(m\phi)+S_{lm}\sin(m\phi)),\quad(1)$$

where G is the gravitational constant; M is the mass of the Moon; R is the Moon's gravity reference radius (1738 km); P_{lm} are the unnormalized associated Legendre polynomial functions of degree l and order m; r, θ, and ϕ are the distance, the colatitude, and the longitude of the evaluation point, respectively; and $C_{l,m}$ and $S_{l,m}$ are the unnormalized SH coefficients at their respective degree and order.

The lunar gravity field recovered by the GRAIL mission, available on NASA's Planetary Data System (PDS), are expressed in the form of normalized SH coefficients ($\bar{C}_{l,m}$ and $\bar{S}_{l,m}$), following the 4π-normalization (i.e., the integral of the harmonic squared equals the area of a unit sphere; Wieczorek & Meschede 2018). They are related to the unnormalized SH coefficients as

$$\begin{pmatrix}C_{l,m}\\S_{l,m}\end{pmatrix}=\left[\frac{(l-m)!(2l+1)(2-\delta_{0,m})}{(l+m)!}\right]^{1/2}\begin{pmatrix}\bar{C}_{l,m}\\\bar{S}_{l,m}\end{pmatrix}.\quad(2)$$

Assuming the coordinate system's origin to be at the center of mass of the Moon, the moment of inertia (I) is described in matrix form as (e.g., Viswanathan et al. 2019)

$$I_{ij}=\begin{bmatrix}I_{11}&I_{12}&I_{13}\\I_{21}&I_{22}&I_{23}\\I_{31}&I_{32}&I_{33}\end{bmatrix}=\frac{C}{MR^2}\begin{bmatrix}1&0&0\\0&1&0\\0&0&1\end{bmatrix}+\begin{bmatrix}C_{20}-2C_{22}&-S_{22}&-C_{21}\\-S_{22}&C_{20}+2C_{22}&-S_{21}\\-C_{21}&-S_{21}&0\end{bmatrix},\quad(3)$$

where C/MR^2 is the polar moment of inertia normalized by the Moon's mass and radius squared; its present-day value, ∼0.39314, is estimated from the analysis of lunar laser ranging data (Viswanathan et al. 2018).

The degree-2 SH coefficients from the GRAIL solution GRGM1200B were used. Since this study focuses on the secular effect of polar wander, we must consider changes to these coefficients from tidal and rotational deformations as a consequence of the evolution of the Earth–Moon orbit over geological timescales. For this, we follow the planetary reorientation theory described in Matsuyama & Nimmo (2009). Their equations (similar to Equations (17) and (26) in Matsuyama et al. 2014) are used to consider the changes to the unnormalized degree-2 SH coefficients ($C_{2,m}$, $S_{2,m}$) from rotational deformation (RD) and tidal deformation (TD), respectively, and are repeated below:

$$\begin{pmatrix}C_{2,m}^{\mathrm{TD}}\\S_{2,m}^{\mathrm{TD}}\end{pmatrix}=(2-\delta_{m0})\frac{(2-m)!}{(2+m)!}\times\left[(k_2^{T*}-k_2^{T})\frac{\Omega^{*2}R^3}{GM}P_{2,m}(\cos\theta_T^*)\begin{pmatrix}\cos(m\phi_T^*)\\\sin(m\phi_T^*)\end{pmatrix}+k_2^{T}\frac{\Omega^2R^3}{GM}P_{2,m}(\cos\theta_T)\begin{pmatrix}\cos(m\phi_T)\\\sin(m\phi_T)\end{pmatrix}\right],\quad(4)$$

$$\begin{pmatrix}C_{2,m}^{\mathrm{RD}}\\S_{2,m}^{\mathrm{RD}}\end{pmatrix}=-(2-\delta_{m0})\frac{(2-m)!}{(2+m)!}\times\left[(k_2^{T*}-k_2^{T})\frac{\Omega^{*2}R^3}{3GM}P_{2,m}(\cos\theta_R^*)\begin{pmatrix}\cos(m\phi_R^*)\\\sin(m\phi_R^*)\end{pmatrix}+k_2^{T}\frac{\Omega^2R^3}{3GM}P_{2,m}(\cos\theta_R)\begin{pmatrix}\cos(m\phi_R)\\\sin(m\phi_R)\end{pmatrix}\right],\quad(5)$$

where m is the order of the SH coefficients, $\delta_{m,0}$ is the Kronecker delta function, k_2^T is the secular (fluid-limit) tidal Love number, Ω is the magnitude of the Moon's rotation vector, GM is the gravitational parameter of the Moon, $P_{2,m}$ are the degree-2 unnormalized associated Legendre functions, and (θ, ϕ) are the spherical coordinates of the rotation (subscript R) and tidal (subscript T) axis, respectively. The components with an asterisk represent the initial components (of the tidal/rotational axes or magnitude of rotation) at epochs without an elastic lithosphere.

In Equations (4) and (5), the terms scaled by $(k_2^{T*}-k_2^{T})$ correspond to the remnant bulge components, while the terms scaled by k_2^T correspond to the equilibrium responses to the forcing rotational and tidal potentials, respectively. This work assumes a 1:1 spin-synchronous history for the Moon as observed today. In Matsuyama et al. (2014), the definition of the (θ_T, ϕ_T) and their corresponding Cartesian unit vectors as noted below their Equation (27) should be read as "tidal" instead of "rotation" axis. We use two sets of values for k_2^{T*} (1.08 and 0.86, corresponding to elastic thickness $T_e=25$ and 50 km, respectively) and $k_2^T=1.44$, following Matsuyama (2013). We consider a frame wherein the equilibrium tidal bulge always points toward Earth ($\hat{u}_x=[1,0,0]$), the equilibrium rotational axis in an orthogonal direction ($\hat{u}_z=[0,0,1]$), and the right-handed triad completed by $\hat{u}_y=[0,1,0]$. The degree-2 components from the rotational and tidal equilibrium deformation thus remain invariant to reorientation in our polar wander calculation.

The orientation of a rotating planet is controlled by the distribution of mass within the planet. The preferred orientation is one in which the energy to maintain the spin is minimum. This means that a planet will prefer to align its spin axis along the maximum moment of inertia to reduce the energy required to keep it spinning. Therefore, such a body in its low-energy (stable) state would align its principal moments along A, B, and C (where $A<B<C$). The moment of inertia of such a body

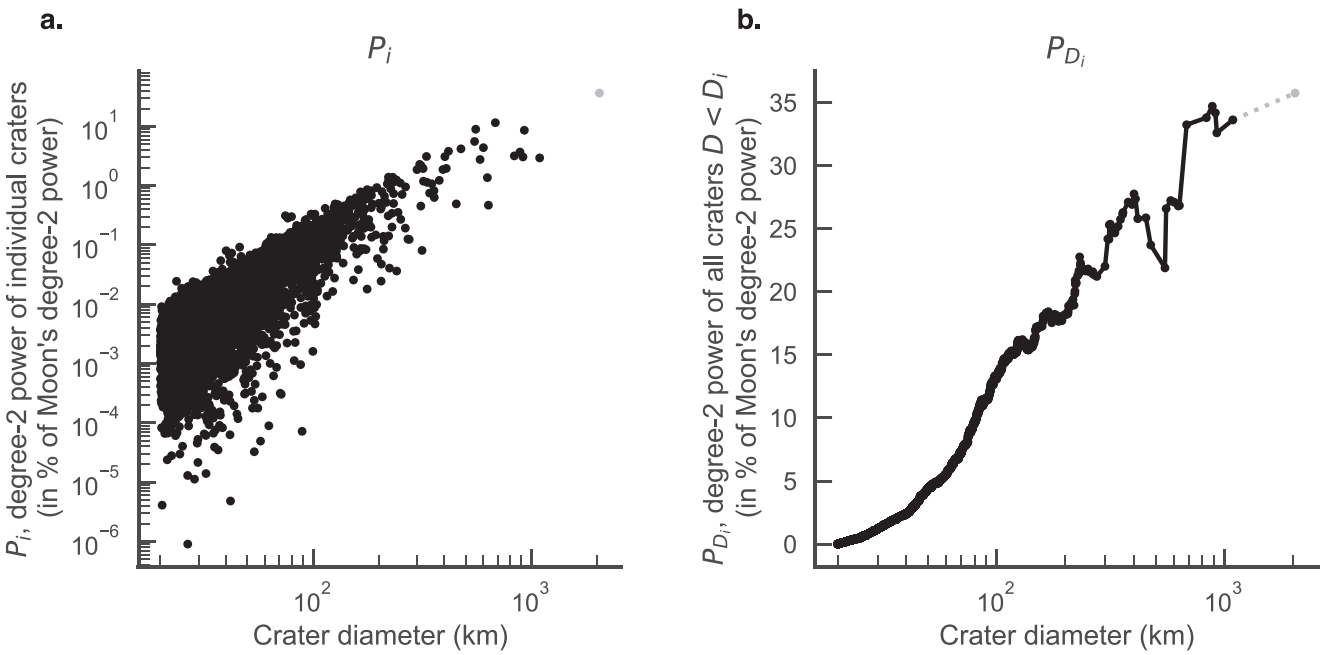

Figure 6. (a) Degree-2 power of the individual SV22 craters sorted by size. Both axis scales are logarithmic. (b) Power of the degree-2 coefficients progressively accumulated by crater size (x-axis scale in logarithmic). The y-axis values are shown normalized to the Moon's full degree-2 power ($\sim 2.045 \times 10^{-4}$). The gray points (one in each of the panels) illustrate the additional consideration of SPA (our model from Table 1).

Table 2
Impact Distribution by Geologic Age Class Shows That the Majority of the Craters Were Assigned to the Pre-Nectarian Period

	Craters by Age Class						
Age Class	1 Pre-Nectarian	2 Nectarian	3 Early Imbrian	4 Late Imbrian	5 Eratosthenian	6 Copernican	Total
Age (Ga)	~4.25–3.91	~3.91–3.85	~3.85–3.80	~3.80–3.2	~3.2–1.1	~1.1–0.1	
Assigned	85	55	9	9	14	12	184
Unassigned	3585	254	211	557	321	88	5013
Total	3670	309	220	566	335	97	5197

Note. Exact numbers would vary slightly between sequence draws, but the ones shown are representative.

would be

$$I_{\mathrm{PA}} = \begin{bmatrix} A & 0 & 0 \\ 0 & B & 0 \\ 0 & 0 & C \end{bmatrix}. \tag{6}$$

Comparing Equations (3) and (6), a body in PA rotation is identified by its $I_{ij:i\neq j} = 0$. Or in terms of SH coefficients of the gravity field, $C_{21} = S_{21} = S_{22} = 0$. This makes finding the PA of a spinning rigid body a matrix diagonalization problem. The eigenvectors of I give the direction cosines that are used to rotate any I into I_{PA}. This also implies that global radially symmetric changes to the moment of inertia tensor (e.g., mean moment $I_0 \equiv (A + B + C)/3MR^2 \equiv C/MR^2 + 2/3C_{20}$) do not contribute to the resulting direction cosines and therefore to polar wander, provided that $A < B < C$. Note that the diagonalization of I_{ij} can yield two *numerical* true polar wander solutions: (1) rotation about the pole, or (2) rotation about the antipole. However, these two solutions cannot be considered *physically* equiprobable. All our polar wander solutions consider the equilibrium rotation to be along the pole (formerly, situated in the northern hemisphere of the Moon), as it leads to relatively smaller and thus more probable, energy-efficient, true polar wander paths.

Anomalies (or a collection of anomalies) that contribute to a nonzero value of the off-diagonal elements of the inertia tensor can drive polar wander. After each anomaly is removed from the present-day gravity field, the residual lunar gravity field is reoriented to the new PA system, while the equilibrium and remnant figures from tidal and rotational deformations continue to remain in the present-day reference frame. This ensures that the initial direction of Earth and the rotation pole remain unchanged in inertial space from these intermediate rotations. This is repeated in an iterative manner over all the anomalies contained in our SV22 catalog.

We cross-validated our implementation using the data provided in Keane & Matsuyama (2014), Keane et al. (2016), and Siegler et al. (2016), resulting in the recovery of their reported paleopoles and polar wander paths. For the evolution of the Earth–Moon system, we evaluated two different evolution models: one based on solid-tidal theory (Mignard 1979; Barnes 2017) and another based on Earth's ocean tidal response (Tyler 2021). The large differences in the tidal and rotational bulges from these very different models

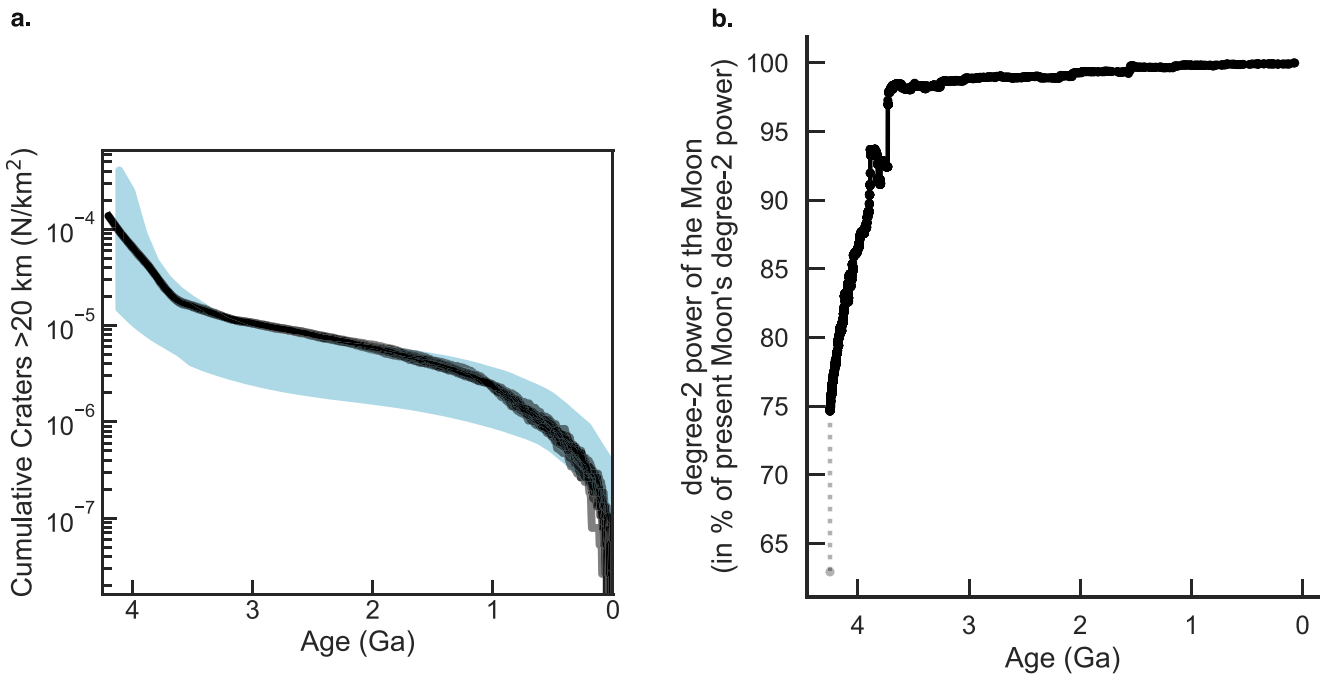

Figure 7. (a) Crater production rates using craters with $D > 20$ km. The shaded area (blue) is obtained after scaling the N(4) values from Heiken et al. (1991) using N(4)/N(20) from Robbins (2019), and the solid lines are the assigned ages in the SV22 catalog. (b) Time history of the power of the Moon's degree-2 coefficients from cratering. The values are shown normalized to the present Moon's full degree-2 power ($\sim 2.045 \times 10^{-4}$). The gray point in panel (b) represents the total after inclusion of our SPA model.

only minimally influenced our polar wander estimates. The results from our computation of polar wander history are discussed in Section 3, with the potential error sources discussed in Section 4.

3. Results

We use the sequencing of the SV22 catalog to remove gravity signatures in order of age to obtain an estimate of the evolution of the polar wander throughout the Moon's history ($\sim$4.25 billion years since the SPA impact).

3.1. Polar Wander History

Using our sequential method for the computation of true polar wander (described in Section 2.3), we trace back the motion of the Moon's pole as it wandered to its present-day location since the SPA formation epoch $\sim$4.25 Ga. Each path shown in Figure 8 corresponds to a single draw of a 5197-crater sequence following the methodology described in Section 2.2. As we will show, the larger steps visible in each trace are the result of the basins ($D > 200$ km). However, the progressive buildup and thus the overall direction (i.e., along the Earth–Moon tidal axis) can be primarily attributed to the cumulative effect of the smaller craters (20–150 km in diameter), in particular because of their nonuniform geographical distribution (see Figure 1(a) and the discussion in Section 3.2).

The first important result is that our estimate of the Moon's paleopole after SPA formation is insensitive to the exact catalog sequence, with final paleopole positions at $\sim$4.25 Ga all close to the rim of a large degraded crater between the present-day Zeeman and Schrödinger craters. The final paleopolar axis of the Moon passes approximately through 80.4° N, 0° E and 80.4° S, 180° E in the northern and southern hemispheres, respectively; the final paleotidal axis passes approximately through 9.6° S, 359° E (near side) and 9.6° N, 179° E (far side). The convergence of all paleopole paths toward the same final paleopole position is due to the near-commutative property of SH coefficients (i.e., invariance to order).

While all our final paleopole positions are practically similar, they contain small differences arising owing to nonlinear effects introduced from the evolving geocentric distance of the Moon over timescales of polar wander. The orbit evolution gives a time-dependent component to the equilibrium tidal and rotational bulges in the polar wander analysis. The assignment of randomized ages (to the features without known ages) also adds to this nonlinearity, as it influences the individual contribution of the feature to polar wander. As per Matsuyama et al. (2014), the magnitude of reorientation would be diminished owing to the opposing action of a remnant bulge with an elastic, unbroken lithosphere of finite rigidity. Therefore, depending on the assigned random age of an impact event, occurring before or after the formation of such a remnant bulge, its contribution to polar wander is expected to be different. We fix the timing of the formation of such a remnant bulge at $\sim$4 Ga following the reference model of Qin et al. (2018) and use it to compute the magnitude of the remnant rotational bulge at those epochs. The total contribution from the above-mentioned nonlinear effects is small in comparison to the reported final paleopole position, of the order of $\sim$0.01° in both longitude and latitude, calculated using the dispersion of the final paleopole positions from the 100 draws. Elastic lithosphere model parameters were fixed for this particular calculation to isolate the contribution from this nonlinear component.

The overall structure, direction, and magnitude of these paleopole paths remain robust when we increase the number of random draws, supporting the interpretation of the near-commutative nature of the small craters' order in our solutions. The net direction of the contribution of 20–200 km diameter craters to polar wander, noticeable during quiescent periods between large impactors, arises primarily as a result of their

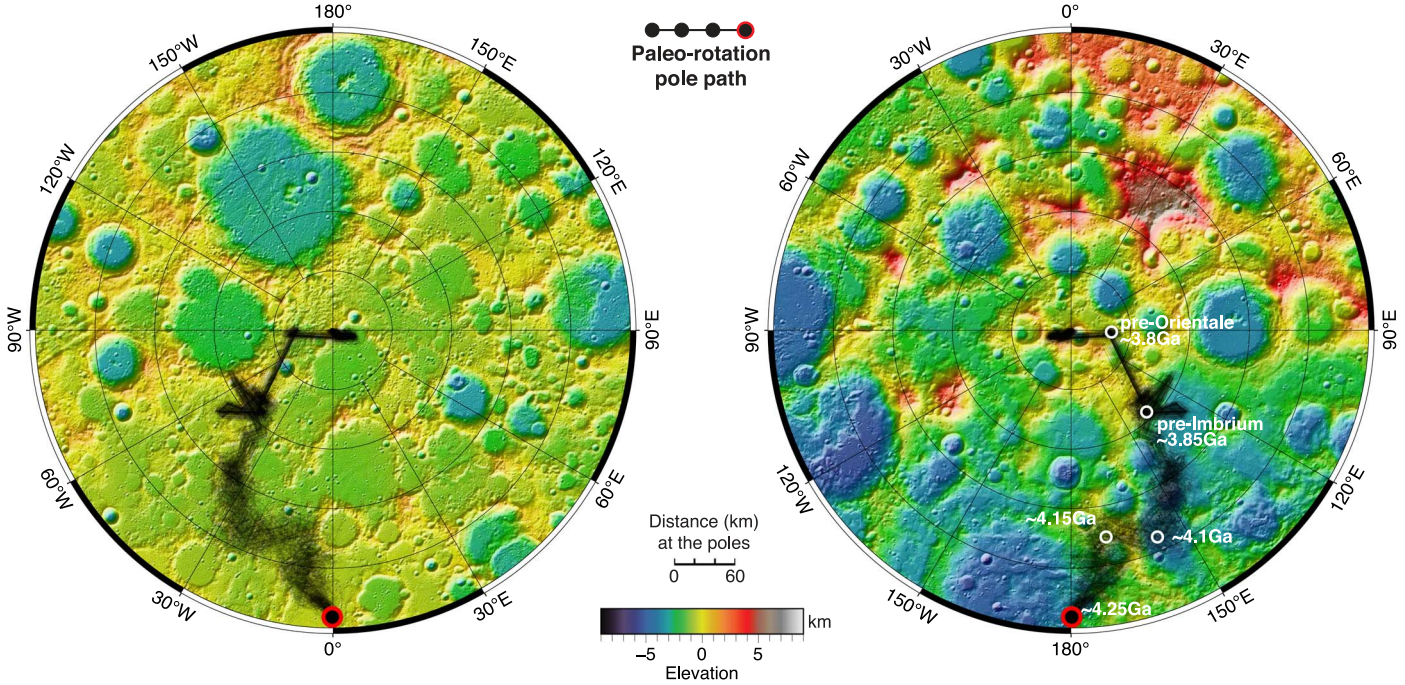

Figure 8. The Moon's polar wander path (black) overlaid on the present-day lunar topography. The stereographic plots are centered at the poles (left: 90° N; right: 90° S) and extend to 80° on the respective hemispheres. The figures show the results from 100 draws, each containing 5197 gravity anomalies of all craters and basins with $D \geqslant 20$ km (except SPA). Time stamps along the polar wander path are marked (white circles). The paleopole positions at ∼4.25 Ga (red circles) are 80.4° N, 0° E and 80.4° S, 180° E (PA reference frame).

global nonuniform spatial distribution. All solutions result in a significant fraction (∼90%) of the total reported pole movement taking place during the first ∼500 Myr after the post-SPA impact, a result of the crater production function and the higher number of craters early in the Moon's history (Table 2).

The geographic location of this paleopole along the Earth–Moon tidal axis implies that the current near-side Procellarum region was ∼10° higher in latitude than it is today, placing the Th-rich deposits and their antipode closer to the poles. Contrary to prior works, this reorientation history opens the possibility that after its formation, SPA was closer to the south pole than it is today. This, however, does not directly or uniquely constrain the relative location of the SPA-forming impact event with respect to the contemporaneous rotational and tidal equatorial bulges. If SPA impacted closer to near-equatorial southern latitude, the large-angle polar wander that it would initiate necessitates a significant readjustment of the tidal and rotational bulges to explain SPA's present-day, higher-latitude location at ∼54° S. Post-SPA impact, as the lunar lithosphere cools and gains some rigidity, such large-angle polar wander becomes restricted, as the induced opposing elastic stresses would prevent a full readjustment of the bulges (Matsuyama et al. 2014). Rather, if SPA impacted closer to the south pole, its contribution to polar wander would be small owing to its high-latitude location as a net-negative anomaly. In this case, SPA would add to the contemporaneous equatorial bulges and increase resistance to the polar wander contribution from subsequent craters and basins. Both cases show that SPA had a major role in the Moon's early reorientation history, acting either as a driver or as an inhibitor to polar wander.

Over the next ∼500 Myr (4.25–3.75 Ga), the Moon was heavily bombarded and the Moon's lithosphere, although relatively less rigid owing to the recently cooled magma ocean, slowly gained the ability to retain some of these cratering signatures in its gravity field (Miljkovic et al. 2021). Large impactors, fewer in number, left large complex gravitational anomalies with an overall net-positive central high (as seen in present-day GRAIL free-air and Bouguer anomaly maps; Neumann et al. 2015). On the other hand, the more numerous smaller impactors contributed smaller, simpler gravitational anomalies with a negative central-low. Overall, the pole position moved to within ∼5° of the present-day pole, with transitions between Early and Late Imbrian geological ages.

At the onset of the Early Imbrian (∼3.85 Ga), the Imbrium-forming impact resulted in a $D \sim 684$ km gravitational anomaly on the Moon's near side, contributing to one of the largest polar and tidal axis surface displacements of about ∼90 and ∼115 km, respectively (Figure 9(a)). We find that the Imbrium basin moved the pole to within ∼2° of the present-day pole. Within the next ∼50 Myr, a similar yet larger gravitational anomaly was left by Orientale, with contributions of ∼85 and ∼20 km along the polar and tidal axis, respectively. The resulting pole movement caused by the Orientale basin-forming impact suggests a trace passing diagonally across the present-day Shackleton crater (see Figure 8). Other major single-event contributors to polar and tidal axis displacements are shown in Figure 9(a). The dispersion of their individual contributions is the result of their changing relative position in the ensemble of 100 sequence draws we considered.

The Moon's paleopole position at ∼3.8 Ga being within ∼2° in latitude of the present-day pole bears on the long-term stability of the lunar polar ice and other volatiles observed in the present-day polar regions (Siegler et al. 2015). Since Orientale's formation, we find that the pole has only moved ∼10% of its full latitude change since post-SPA. This suggests that the polar cold traps observed today could have been relatively stable for polar volatile accumulation since the beginning of the Late Imbrian provided little obliquity change

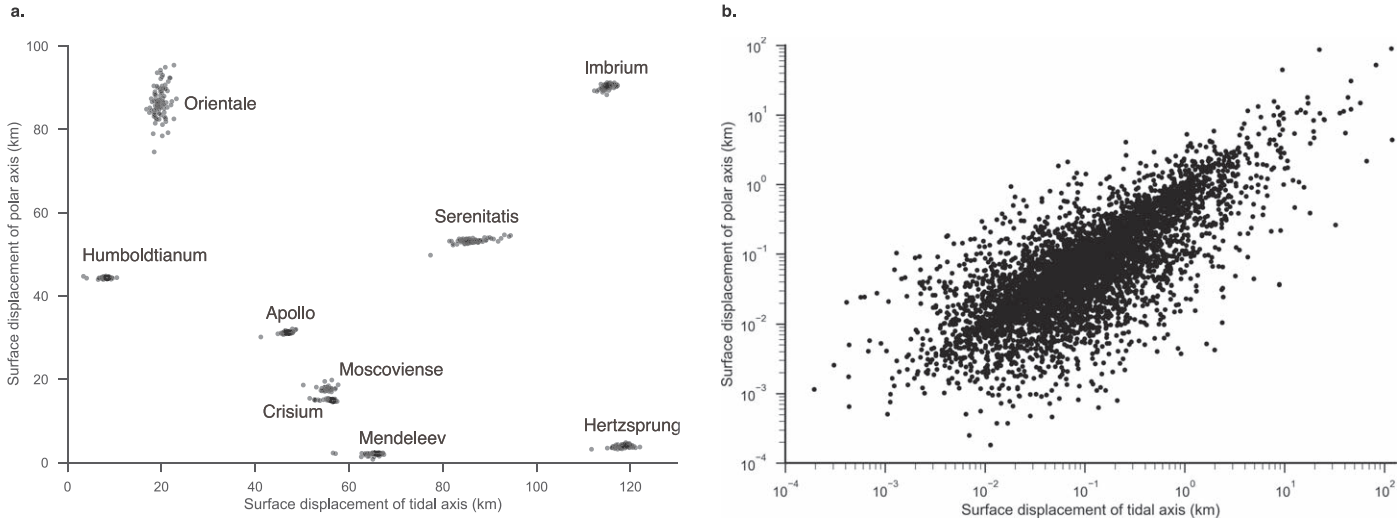

Figure 9. (a) Surface displacements along the polar and tidal axis from large craters and basins, realized using 100 draws. Dispersion comes from relative positioning in the cratering sequence. A subset is selected here based on impact events that resulted in the displacement of the tidal axis (⩾50 km) or polar axis (⩾20 km) at the surface. (b) Surface displacements along the polar and tidal axes from all SV22 craters, realized using a single draw. Note the strong correlation between displacements along the tidal and polar axes.

during that time. This also implies that any volatiles released by post-Orientale basin volcanism and reaching polar cold traps would be sequestered in any crater existing at that time in the current circumpolar region, including some currently at latitude 75° S.

The effect of the small craters is more prominent during quiescent periods between large impactors. Individually, their median contributions to pole displacements measured at the surface are relatively small, of the order of tens of meters for 25 km $\geqslant D \geqslant$ 20 km (Figure 9(b)). Similarly, a crater such as Tycho, with $D \sim 82$ km, can only cause displacements of the order of ∼1 km. However, their collective influence cannot be neglected, as they show a consistent directionality that influences the pole movement. This displacement direction is invariant from their relative timing in the catalog sequence, adding to the robustness of this study. Indeed, it is the nonuniform geographical distribution of such small craters that is the prime reason for their overall directional influence on polar wander, as evidenced in the present-day gravity field and topography (recall Figure 1).

3.2. The Role of Small Craters

The distribution of craters on the Moon is far from uniform as is evident in Figure 1(a). Areas in the mare regions, such as Procellarum, and around large basins, such as Orientale, show strong deficits. A full discussion of the distribution of these craters can be found in Head et al. (2010), but we note that this indicates that their collective contribution to lunar gravity is unlikely to cancel and accumulate to zero. This nonuniformity and imbalance in distribution is also clear when viewed in the histograms of Figure 10. The latitude distribution is showing a deficit in the northern hemisphere (Figure 10). Similarly, fewer small craters are located in the ∼240°–60° E longitude band, illustrating the deficit in the mare and Orientale regions and the presence of the heavily cratered far-side highlands (Evans et al. 2018).

We demonstrate the importance of this nonuniform distribution of the small craters (5073 craters with $D < 150$ km) for the final paleopole position in three different ways.

First, we computed paleopole estimates using only the same large craters ($D > 207$ km) considered by Keane & Matsuyama (2014). We obtain a final paleopole in the same quadrant (180°–270° E, in the northern hemisphere), similar to the findings of Keane & Matsuyama (2014). This cross-validation of our approach with theirs, both in the reorientation methodology and in the gravity signature modeling (within their reported error bars, as previously shown in Figure 5), clearly attributes the large differences in longitude (90° or more) of our complete-catalog estimate to the effect of neglecting the influence of small impact features.

Second, we conducted a synthetic test to evaluate the influence of the small craters on the final paleopole longitude. We created synthetic Moons by rotating only the small-crater ($D < 200$ km) population through 0–360° by 30° increments in their longitudes, while leaving all the larger craters fixed in their current positions. The left panel of Figure 11 shows the final paleopole positions obtained from such synthetic Moons; the changes in the longitude of the final paleopoles are clearly driven by the small-crater population distribution. The small elongation is attributed to the influence of the underlying ellipsoid's nonzero C_{22} component.

Third, we conducted a statistical test to rule out random walk as the reason for our final paleopole position. The observed nonuniform distribution of small craters gives a pole movement of ∼6° in latitude along 225° E (at the southern hemisphere), or 45° E in the north as shown in Figure 11 (white circle, right panel). We compared this to the results obtained from hypothetical random distributions of small craters. We created 10,000 small-crater catalogs where their coordinates (latitude and longitude) were randomized. For each, we computed a final paleopole position, and we report in the right panel of Figure 11 their distribution as a two-dimensional histogram. The typical change in latitude is ∼1.35°, indicating that the paleopole estimate from the actual catalog is clearly a robust signal (>99.9% C.I.). The slight longitudinal preference at 90° E and 270° E comes from the underlying ellipsoid's C_{22} (as identified before), but it is offset by ∼45° from the observed paleopole and thus is not a cause. Further randomizations of both longitude and latitude (considered separately) of the

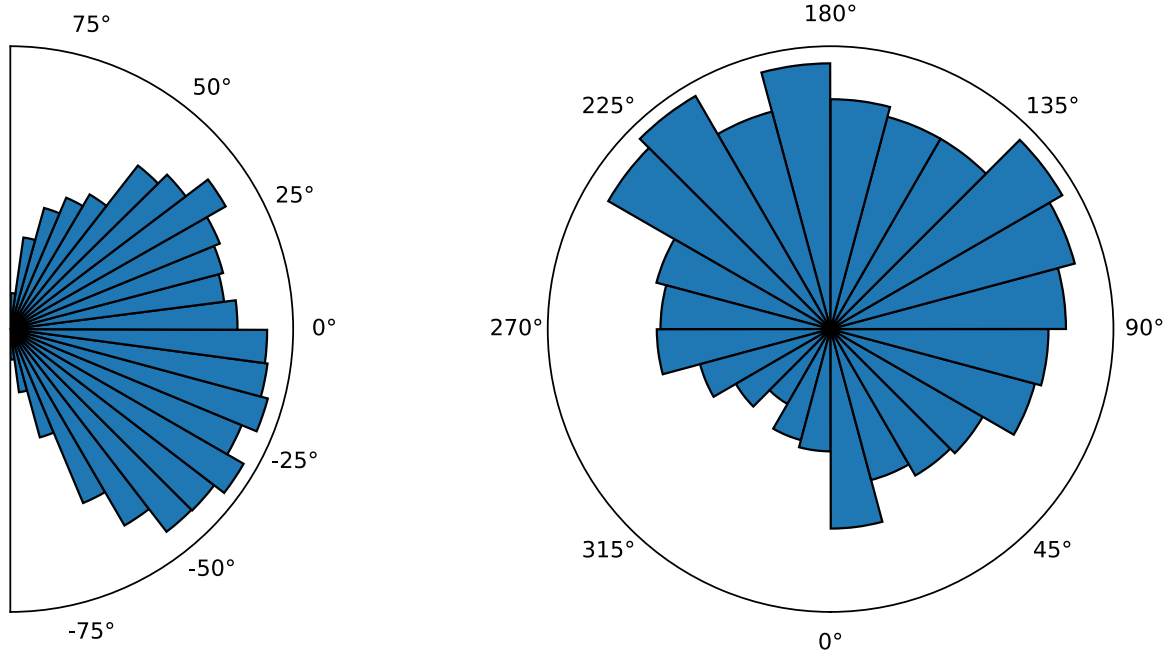

Figure 10. Distribution of craters 20–150 km in diameter as a function of latitude (left) and longitude (right). The distribution in latitude shows the north with fewer craters than the south in the latitude range 0°–25°, while the longitude distribution (right) shows a significant bias toward the 90°–240° longitudes. Latitude bins are not normalized by surface area; any north–south asymmetry would remain invariant to such normalization.

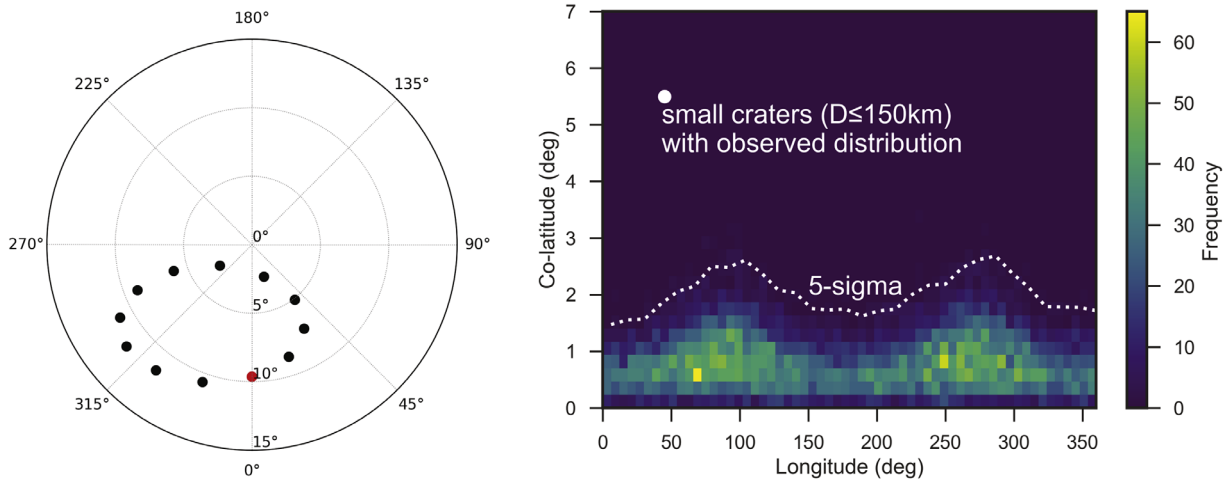

Figure 11. Left: north final paleopole positions using the observed distribution of all 5197 craters (in red; without SPA) and 30° longitude increments on small-crater ($D < 200$ km) positions (in black). Right: comparison of the final paleopole position from a subset of 5073 small craters ($D \leqslant 150$ km) using their observed distribution (white circle) vs. 10,000 draws of their randomized latitudes and longitudes (bins). The dotted curve represents the 5σ standard deviation of the final paleopole colatitude from the 10,000 draws considered for this statistical test. The pole movement due to the observed, nonuniformly distributed small craters has a high statistical significance and should thus not be considered an effect of random walk.

small-crater population also give similar results, ruling out random walk on polar wander along both dimensions.

These three lines of evidence provide a consistent takeaway message, that because of its nonuniform distribution the small-crater population is a significant cause of true polar wander.

4. Discussion

In this section we discuss comparisons of the degree-2 power with prior work, potential sources of uncertainties in our pole path reconstruction, and how we dealt with them in our solutions.

Comparisons of degree-2 power with prior work based on the gravity field. SPA has been said to account for the overwhelming majority of the gravitational flattening (C_{20}) and by implication to entirely drive the polar wander evolution. For instance, Keane & Matsuyama (2014) stated that SPA accounted for 96% of the total degree-2 power from the mass anomalies. Here "the mass anomalies" refer to the ∼30 craters they considered and not the total degree-2 power in the free-air anomaly of the Moon as observed by GRAIL. Unfortunately, recent work by Matsuyama et al. (2021) again focused on SPA exclusively, assuming that all other features were minor, and claimed that SPA accounted for 96% of the total degree-2 power from (all) mass anomalies. Rather, if all mass anomalies were considered, SPA's contribution would be only ∼46% with respect to the total degree-2 power. Our study emphasizes

that small craters are a significant contributor to polar wander and should not be ignored. We also note that there is an important distinction between the comparison of individual C_{20} and degree-2 power (P_i) versus cumulative degree-2 power (P_{D_i}). Modeling differences of the SPA gravity signature can lead to large variations in its individual power to the Moon's: 36% in our SPA model, 46% for Keane & Matsuyama (2014), 62% for Matsuyama et al. (2021). However, when cumulative degree-2 power is considered, the non-SPA craters and basins account for 34% (ours with ∼5000 craters) and 27% (Keane & Matsuyama 2014, with 30 craters) of the Moon's power, on a par with SPA alone.

Crater gravity anomaly modeling and extraction.—In general, pole path reconstruction results depend primarily on the accuracy of the model representing the gravity anomalies. In our case, these models are derived directly from the GRAIL gravity model (GRGM1200B solution; Goossens et al. 2020) as described in Section 2.1. Using $r_i > 1.75R_i$ instead of $r_i > 1.25R_i$ for the background gravity removal resulted in ∼10% change on the degree-2 coefficients of the larger craters with minimal change on the craters with $D < 200$ km. A total of ∼1° error on the final paleopole position is noted from this choice. We compared our method for the 29 largest craters with previous estimates (Keane & Matsuyama 2014; Keane et al. 2016) for the degree-2 coefficients and showed that our models agreed within 3σ for 27 out of the 29 large craters (recall Figure 5). Further, Figure 5 also showed that the agreement for the smaller craters was 100% within 3σ, providing confidence that we could extend our approach to a much larger number of smaller crater anomalies. Additionally, we quantified the potential residual anomaly errors introduced by our crater modeling and extraction procedure. For this, we created a synthetic lunar gravity field (with the C_{20} and C_{22} from GRGM1200B) and introduced synthetic craters based on the SV22 catalog, such as original position, diameter ($D \leqslant 200$ km), and central free-air anomaly. Extraction of these 5130 synthetic craters using our methodology results in a relative error of ⩽2% on the recovery of the total underlying degree-2 equilibrium figure (<2% on C_{20} and <0.5% C_{22}). These errors are reduced to <0.0015% when considering only a subset of ∼100 craters ($D \leqslant 20.5$ km) with no significant overlaps, which further demonstrates that the recovery procedure itself does not alter the underlying degree-2 figure. Note that for this test we purposely used a different method for the modeling of the synthetic craters (using spherical caps) versus the method for the modeling for the extracted craters (as described in Section 2.1). Hence, the errors noted above should be considered to be slightly pessimistic.

Crater size and anomaly magnitude.—We use the GRAIL gravity field to resolve crater anomaly signatures down to 20 km in diameter. The gravity signal at 20 km is over 2 orders of magnitude greater than the GRAIL field accuracy, and the correlation of topography with free-air gravity is 98% on the lunar near side and over 99% on the lunar far side (Zuber et al. 2013a). This indicates that the act of gravity modeling of small craters from a Kaula-constrained ($L > 600$) gravity solution of GRAIL, even down to 20 km in diameter, does not constitute an appreciable source of error.

Anomaly ages.—We used the crater production rate to estimate the crater frequency within each geologic group. The ordering of the anomalies based on its age has a minimal effect on the final position of the paleopole but can have a significant effect on the pole path if left unconstrained. Our crater age assignment leverages the best-known age estimates for the large craters and basins to minimize this error (recall Section 2.2). The single largest lunar reorientation event in our analysis, ∼4° along ∼30° W and ∼150° E (left and right panels of Figure 8, respectively), occurred at ∼3.9 Ga (age estimate from Merle et al. 2014) from the formation of the Imbrium basin. On the contrary, small craters (20 km ⩽ $D < 150$ km) individually contribute to a median pole movement of ∼3″ on latitude. Since their distribution is spatially nonuniform and their ages are less certain, they can carry forward errors in a preferential direction onto the pole path if their age distribution deviates significantly compared to the age distribution of the larger craters. However, the database of Losiak et al. (2009) shows that craters with known age classes within 20 km ⩽ $D < 100$ km are present across all age classes (1 through 6). A preferential depletion of the impactor population in the vicinity of the early Earth–Moon system, based on diameter alone, may also be unfounded. Due to these reasons, our age assignment presumes both small and large craters to follow the crater production rate curves of Figure 7(a). Under this presumption, our 100 draws of random crater distributions provided a series of pole traces that resulted in the overall minimal dispersion as shown in Figure 8.

Completeness of crater catalog.—The list of small-crater anomalies is based on their identification in LOLA topography (Head et al. 2010). We recognize that other crater lists (e.g., Losiak et al. 2009; Robbins 2019) could have been used and that craters with $D < 20$ km could be an additional source of polar wander not accounted for in this study. However, we note that mapping smaller craters close to or below the GRAIL effective resolution should be performed with caution, as our internal tests show that such an attempt could introduce nonzero systematic biases in the individual anomaly magnitude that quickly scales with crater frequency (see Figure 2).

Time evolution of small-crater distribution.—We note that the asymmetrical distribution in the currently observed crater population is primarily due to selective erasure of craters due to mare volcanism on the near side in the Oceanus Procellarum region. While the original distribution is expected to have been close to uniform, we do not have access to such a crater catalog and are not able to assign ages of formation and erasure to account for these in our backward integration. Evidence from the majority of model ages of the lunar mare basalts (Hiesinger et al. 2010) and the estimated peak of volcanic eruption rate (Head & Wilson 1992) suggests that such global asymmetry existed since early in the Moon's history. On the other hand, radiometric dating of samples from the recent Chang'e-5 mission gives ages closer to ∼2 Ga (Che et al. 2021; Li et al. 2021), suggesting that more recent small-crater erasure may be localized in parts of Oceanus Procellarum. Both these age estimates indicate that the asymmetry has persisted for at least ∼2 billion years and more likely since the end of the Late Imbrian (Wilhelms et al. 1987, Plates 9–10). For earlier epochs, the paleopole path may have been different owing to missing information about formation and subsequent erasure of a subset of the crater population. Nevertheless, because of the near invariance from the relative sequence order noted earlier, these counteract each other. Our final paleopole is thus robust to the effects of formation and erasure of currently unobserved craters. Future work will seek to bound the possible departures

from our current paleopole path in the period from ∼2 or ∼3.5 Ga to ∼4.25 Ga.

Tides and the evolution of the Earth–Moon distance.—We employed the solid-tide model in Barnes (2017; based on Mignard 1979) for the evolution of Earth–Moon distance and the corresponding lunar rotation rate (assuming a 1:1 spin-synchronous Moon). We also used solutions from Tyler (2021), which were based on Earth's ocean tidal response. The differences between both models had minimal effect on our paleopole positions. Other spin-synchronous modes capable of modifying the remnant tidal and rotational bulges were not explored, as the remnant bulges themselves (terms scaled by $(k_2^{T*} - k_2^T)$ in Equations (4) and (5)) had minimal effect on our ∼10° pole movement.

Other gravitational signatures.—Any change in mass distribution can contribute to planetary reorientation. Our work represents a first comprehensive effort that includes all craters and basins with 20 km $\leqslant D <$ 1200 km. Several other near-surface gravitational features (e.g., SPA, smaller craters, lunar mare) and other plausible internal phenomena (e.g., degree-1 mantle convection from localized radioactive heat sources; Laneuville et al. 2013) were not considered in this study given that they are active and yet-unresolved research topics. Prior works considered some of these other gravitational signatures individually. A more comprehensive effort should involve combinations of several of these features rather than an individual consideration. The error associated with such combinations remains unknown and is left for future investigations.

5. Conclusions

The primary objective of this study was to assess the likely contribution from the thousands of small craters to the evolution of the Moon's gravitational flattening and pole movement. We have estimated the polar wander of the Moon from the gravitational contribution of 5197 craters and basins with 1200 km $> D \geqslant$ 20 km as recorded in the present-day GRAIL gravity field. Our results show that the abundance and nonuniform distribution of 20–200 km craters make them a critical contributor to polar wander and thus that they should be considered in any planetary reorientation study. The method of extracting gravity anomalies numerically, rather than by geophysical modeling, has enabled the inclusion and modeling of large numbers of smaller craters with a good accuracy. The sequential treatment of each anomaly in age order results in an updated pole location after each subtraction and enables the derivation of an approximate pole path since the SPA impact.

Previous reconstructions of lunar polar wander using gravity field neglected the contribution of craters smaller than 200 km to the degree-2 gravity field of the Moon. When these smaller craters are included, we find the following:

1. A net displacement of the Moon's pole by ∼10° in latitude in the general direction of the present-day Earth–Moon tidal axis with the paleopole coordinates post-SPA at ∼80° N/S, 0/180° E.
2. Most of this true polar wander occurs post-SPA in the Late Nectarian and Early Imbrian Period (pre-Orientale; Figure 8) and places the post-SPA south pole on the edge of the ∼140 km diameter De Forest crater located at 80.8° S, 191.2° E. The geographic location of this paleopole along the Earth–Moon tidal axis implies that the current near-side Procellarum region was ∼10° higher in latitude than it is today, placing the Th-rich deposits and their antipode closer to the poles.
3. Since the Orientale impact, the pole has only moved ∼10% of its full latitude change since post-SPA and has passed through the Shackleton crater before arriving at its present-day location.
4. This suggests that the polar cold traps could have been relatively stable for polar volatile accumulation since the beginning of the Late Imbrian provided that there has been little change in the lunar obliquity during that time. This also implies that any volatiles released by post-Orientale basin volcanism and reaching polar cold traps would be sequestered in any crater existing at that time in the current circumpolar region, including some currently at latitude ∼75° S.

The authors gratefully acknowledge the support of the Lunar Reconnaissance Orbiter project to the LOLA investigation for this study. Support for this research was provided by NASA's Planetary Science Division Research Program. Portions of this material are based on work supported by NASA under award Nos. 80NSSC18K0553 (MIT; contributions from D.E.S.), 80GSFC17M0002/80GSFC21M0002 (UMBC-CRESST II; contributions from V.V. and S.G.), and 80NSSC19K0605 (Brown; contributions from J.W.H.). Open-source packages used for this study include SHTools for operations on SH coefficients (Wieczorek & Meschede 2018), Astropy for constants and coordinate transformations (The Astropy Collaboration et al. 2018), and seaborn, GMT, and matplotlib for graphics (Waskom 2021; Wessel et al. 2019; Hunter 2007). The authors thank T. J. Sabaka (GSFC) and R. H. Tyler (UMBC/GSFC) for discussions. We thank the anonymous reviewers for their suggestions that helped improve the clarity of the work presented and E. G. Rivera-Valentín for the editorial handling of our manuscript. The GRAIL gravity and LRO-LOLA topography data sets used in the study are available on NASA's Planetary Data System Geosciences Node at https://pds-geosciences.wustl.edu/missions/grail/default.htm and https://pds-geosciences.wustl.edu/missions/lro/lola.htm, respectively.

ORCID iDs

David E. Smith https://orcid.org/0000-0003-3104-2169
Vishnu Viswanathan https://orcid.org/0000-0002-9027-8588
Erwan Mazarico https://orcid.org/0000-0003-3456-427X
Sander Goossens https://orcid.org/0000-0002-7707-1128
James W. Head https://orcid.org/0000-0003-2013-560X
Gregory A. Neumann https://orcid.org/0000-0003-0644-9944
Maria T. Zuber https://orcid.org/0000-0003-2652-8017

References

Asmar, S. W., Konopliv, A. S., Watkins, M. M., et al. 2013, SSRv, 178, 25
Barnes, R. 2017, CeMDA, 129, 509
Bills, B. G. 1995, JGR, 100, 26297
Che, X., Nemchin, A., Liu, D., et al. 2021, Sci, 374, 887
Chin, G., Brylow, S., Foote, M., et al. 2007, SSRv, 129, 391
Evans, A. J., Andrews-Hanna, J. C., Head, J. W., et al. 2018, JGRE, 123, 1596
Evans, D. 2002, Tectp, 362, 303
Fassett, C. I., Head, J. W., Kadish, S. J., et al. 2012, JGRE, 117, E00H06
Garrick-Bethell, I., Miljkovic, K., Hiesinger, H., et al. 2020, Icar, 338, 113430
Garrick-Bethell, I., Perera, V., Nimmo, F., & Zuber, M. T. 2014, Natur, 512, 181

Goossens, S., Sabaka, T. J., Wieczorek, M. A., et al. 2020, JGRE, 125, e06086
Head, J. W., Fassett, C. I., Kadish, S. J., et al. 2010, Sci, 329, 1504
Head, J. W., & Wilson, L. 1992, GeCoA, 56, 2155
Heiken, G. H., Vaniman, D. T., & French, B. M. 1991, Lunar Sourcebook, A User's Guide to the Moon (Cambridge: Cambridge Univ. Press)
Hiesinger, H., Head, J. W., Wolf, U., Jaumann, R., & Neukum, G. 2010, JGR, 115, E03003
Hunter, J. D. 2007, CSE, 9, 90
Kaula, W. M. 1966, Theory of Satellite Geodesy: Applications of Satellites to Geodesy (Waltham, MA: Blaisdell Publishing Co.)
Keane, J., Johnson, B., Matsuyama, I., & Siegler, M. 2017, AGUFM, 2017, P11F–04
Keane, J. T., & Matsuyama, I. 2014, GeoRL, 41, 6610
Keane, J. T., Matsuyama, I., Kamata, S., & Steckloff, J. K. 2016, Natur, 540, 90
Laneuville, M., Wieczorek, M. A., Breuer, D., & Tosi, N. 2013, JGRE, 118, 1435
Li, Q. -L., Zhou, Q., Liu, Y., et al. 2021, Natur, 600, 54
Losiak, A., Wilhelms, D., Byrne, C., et al. 2009, LPSC, 40, 1532
Matsuyama, I. 2013, Icar, 222, 411
Matsuyama, I., & Nimmo, F. 2007, JGR, 112, E11003
Matsuyama, I., & Nimmo, F. 2009, JGR, 114, E01010
Matsuyama, I., Nimmo, F., & Mitrovica, J. X. 2014, AREPS, 42, 605
Matsuyama, I., Trinh, A., & Keane, J. T. 2021, PSJ, 2, 232
Melosh, H. J. 1975, E&PSL, 26, 353
Merle, R. E., Nemchin, A. A., Grange, M. L., Whitehouse, M. J., & Pidgeon, R. T. 2014, M&PS, 49, 2241
Mignard, F. 1979, M&P, 20, 301
Miljkovic, K., Wieczorek, M. A., Laneuville, M., et al. 2021, NatCo, 12, 1
Morbidelli, A., Nesvorny, D., Laurenz, V., et al. 2018, Icar, 305, 262
Nayak, M., Hemingway, D., & Garrick-Bethell, I. 2017, Icar, 286, 153
Neukum, G., Ivanov, B. A., & Hartmann, W. K. 2001, SSRv, 96, 55
Neumann, G. A., Zuber, M. T., Wieczorek, M. A., et al. 2015, SciA, 1, e1500852
Qin, C., Zhong, S., & Phillips, R. 2018, GeoRL, 45, 1286
Robbins, S. J. 2019, JGRE, 124, 871
Shapiro, I. I., Chandler, J. F., Murphy, T. W., & Reasenberg, R. D. 2021, JGRE, 126, e06887
Siegler, M., Paige, D., Williams, J. -P., & Bills, B. 2015, Icar, 255, 78
Siegler, M. A., Miller, R. S., Keane, J. T., et al. 2016, Natur, 531, 480
Smith, D. E., Zuber, M. T., Jackson, G. B., et al. 2010a, SSRv, 150, 209
Smith, D. E., Zuber, M. T., Neumann, G. A., et al. 2010b, GeoRL, 37, L18204
Takahashi, F., Tsunakawa, H., Shimizu, H., Shibuya, H., & Matsushima, M. 2014, NatGe, 7, 409
The Astropy Collaboration, Price-Whelan, A. M., Sipőcz, B. M., et al. 2018, AJ, 156, 123
Tyler, R. H. 2021, PSJ, 2, 70
Viswanathan, V., Fienga, A., Minazzoli, O., et al. 2018, MNRAS, 476, 1877
Viswanathan, V., Rambaux, N., Fienga, A., Laskar, J., & Gastineau, M. 2019, GeoRL, 46, 7295
Waskom, M. 2021, JOSS, 6, 3021
Wessel, P., Luis, J. F., Uieda, L., et al. 2019, GGG, 20, 5556
Wieczorek, M. A., & Meschede, M. 2018, GGG, 19, 2574
Wilhelms, D. E., McCauley, J. F., & Trask, N. J. 1987, The Geologic History of the Moon, Professional Paper, 1348, USGS
Williams, J. G., & Boggs, D. H. 2021, JGRE, 126, e06920
Zuber, M. T., Smith, D. E., Lehman, D. H., et al. 2013a, SSRv, 178, 3
Zuber, M. T., Smith, D. E., Watkins, M. M., et al. 2013b, Sci, 339, 668